Contents lists available at ScienceDirect

Heliyon

journal homepage: www.cell.com/heliyon

Research article

3D design and analysis of an electro-optically tunable athermal and polarization-insensitive ring resonator-based add-drop filter for DWDM systems

Filston Rukerandanga [a,*], Stephen Musyoki [b], Edwin O. Ataro [b]

[a] Department of Electrical Engineering, Pan African University, Institute for Basic Sciences, Technology and Innovation, P.O. Box 62000-00200, Nairobi, Kenya
[b] School of Electrical and Electronic Engineering, The Technical University of Kenya, P.O. Box 52428, 00200 Nairobi, Kenya

ARTICLE INFO

ABSTRACT

Dense Wavelength Division Multiplexing system-based optical networks are currently the most appropriate solutions for all-optical networks that efficiently utilize the large bandwidth offered by optical fiber networks. Tunable ring resonator-based filters are highly attractive owing to their bandwidth and channel tunability, high spectral selectivity, low losses, low power consumption, and compactness; thus they are very good candidates for optical integrated circuits at a very large scale. We used titanium oxide and silicon oxide as the upper-cladding and under-cladding materials, respectively, around a silicon-rich nitride core to design an electro-optically tunable, polarization-insensitive, and thermally resilient sixth-order add-drop optical filter in the L-band (1565 nm-1625 nm). A thin film of lithium niobate added on the top of silicon oxide was used to enhance the tunability of the filter. A 3D multiphysics approach considering thermo-optic, and stress-optical effects while minimizing the polarization rotation has been adopted to solve the electromagnetic problem in a filter that can accommodate arbitrary Transverse Electric and Transverse Magnetic polarized optical signals. The device has a bandwidth of 50 GHz (linewidth of 0.4 nm) at a resonant wavelength of 1575.4 nm, an extended FSR of 2.512 THz, and losses of 0.82 dB in the bandpass. The filter is ultra-compact with a footprint of 15 μm × 160 μm. We achieved a high-quality factor of 3250, a tunability efficiency of 8.95 pm/V, and a finesse of 31. To the best of our knowledge, it is the first time a complementary metal-oxide-semiconductor-compatible, electro-optically tunable, athermal, polarization-insensitive high order add-drop filter in the L-band with a top-flat response in the passband, and with an extended FSR has been designed for Dense Wavelength Division Multiplexing systems.

1. Introduction

Dense Wavelength Division Multiplexing (DWDM) systems represent the main techniques used in the realization of flexible optical networks (FONs) and all-optical networks [1][2]. These techniques, coupled with Erbium-Doped Fiber Amplifiers (EDFAs), are currently used in the C-band (1530-1565 nm) where optical fiber losses are the lowest and with an increasing interest in the less occupied L-band (1565-1625 nm) [3]. With equal importance with wavelength selective optical sources, optical filters are key elements in Wavelength Division Multiplexing (WDM) systems for selection, routing, adding and dropping specific wavelengths [4]. A tunable add-drop filter is the basic building block of DWDM systems, because it must ensure an accurate wavelength selection for isolating different channels [5]. In addition, for

DWDM systems, tunable filters must ensure a wide free spectral range (FSR) such that the spacing between frequencies can accommodate the set of WDM channels within a telecommunications window [6][7].

Different optical filter technologies such as Arrayed Waveguide Gratings (AWGs) [8], Micro-Electro-Mechanical Structural (MEMS) filters [9][10], Thin Films (TF) filters [11], Mach-Zehnder Interferometers (MZI) filters [12], Fiber-Bragg Gratings (FBG), and Fabry-Perot (FP) filters [13][14], have been reported in the literature. Although the characteristics of ring resonator-based filters are very similar to those of Fabry-Perot cavity-based optical filters, their design does not require facets or gratings and offers the advantage that the injected and reflected signals are separated into individual waveguides, and thus are particularly simple to design [15]. In DWDM systems, they offer the advantages over various other filter technologies mentioned earlier in the

---

text: low insertion loss (IL), low power consumption, high sidelobe suppression, large dynamic range, fast tuning speed, simple control mechanism, mass production possibility, low price, and ultra-compactness, and therefore are very well suited for large-scale integration [16][17].

Silicon-based ring resonators filters directly inherit from silicon photonics various benefits such as high bandwidth, mature fabrication techniques, smaller size, reliability enhancement, CMOS compatibility, low-energy consumption, and nonlinear enhancement compared to classical electronic technology [18]. Many material systems such as silicon-on-insulator (SOI) [19], silicon nitride (SiN) [20], Lithium Niobate-on-insulator (LNOI) [21], germanium-on-silicon (Ge-Si) [22], and III–V materials on-silicon [23], have been used for various applications including sensing, switching, routing, and filtering. Among these platforms, the high-index contrast of the Silicon On Insulator (SOI) material system allows strong field confinement with small radii down to 2.5 μm but comes with increasing bending losses and polarization rotation problems [19]. In addition, particular attention must be paid to controlling the instability of these devices owing to temperature variations.

Scientists are still extensively researching ring resonator-based optical filters and are trying to improve the performance in one or more of the following performance criteria with regard to the application: insertion losses [24], bending losses [25], size [26], channel spacing [27], free spectral range (FSR) [28], full wave half maximum (FWHM), quality (Q) factor, extinction ratio [29], cross-talk, tuning range, tuning speed [30], thermal dependence and polarization sensitivity [31][32][33]. Solutions have been proposed to reduce polarization sensitivity and thermal instability [7][31][34]. In fact, a tantalum pentoxide (Ta_2O_5)-based athermal micro-ring resonator has been designed with a propagation loss of 0.56 dB/cm, a Q factor of 5000 and a large radius of 50 μm [33]. Microring resonators (MRRs) in linear materials such as silicon-lithium niobate [30] and nonlinear materials, such as silicon-graphene [35][4] show a great potential for providing tunable filters without addressing the temperature and polarization dependence behavior. An add-drop filter based on a TiO_2-cladded amorphous-SOI with an athermal behavior in the range of 60 nm is reported, and a CMOS-compatible athermal and polarization-insensitive racetrack resonator as a photonic notch filter is proposed in the C-band but is not tunable [32].

This work is concerned with the design of an athermal polarization-insensitive high-order, tunable add-drop filter, with a stable resonant wavelength in the L-band and extended FSR for DWDM systems. The design intends to appropriately choose materials, dimensions, and shape of the waveguides to mitigate polarization and thermal fluctuations in the CMOS-compatible device while maintaining very low losses and power consumption according to an International Telecommunication Union (ITU) recommendation on a flexible grid for channel spacing in (Dense) Wavelength Division Multiplexing [6]. Thus, temperature and polarization control systems are avoided enabling a less complex and lower energy-consuming device. In this research, a multiphysics approach enabled us to include simultaneously many physical phenomena such as thermo-optic, stress-optical, and electro-optical effects. In addition, analysis, design, modeling, and simulation were carried out on serially coupled ring resonators as a topology owing to its effectiveness in realizing flat-top and steeper frequency responses.

2. Materials and methods

As mentioned in Section 1, a multiphysics approach was used to consider various physical aspects of the study, as it involves different physics and engineering fields to create conditions close to the real operational conditions in a Photonic Integrated Circuit (PIC) setting. Coupled Mode Theory (CMT) was used to determine the coupling coefficients and transfer functions of a maximally flat-response filter in the L-band. The coupled-mode equations were solved using MATLAB software. The design of the filter geometry and simulations were
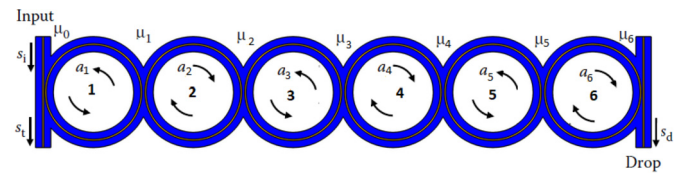

Fig. 1. Top view of a six-ring-based serially coupled add-drop filter.

continuously carried out using COMSOL Multiphysics software, considering thermo-optic, stress-optical, and electro-optical effects in the structure of the device. To investigate those effects, Heat Transfer in Solids physics, Solid Mechanics physics coupled to thermal expansion multiphysics, and Electrostatics physics interfaces, respectively were incorporated. The Finite Element, Beam Envelope Propagation Method was used to solve the electromagnetic problem in the model using the Electromagnetic Waves, Beam Envelopes interface. The targeted spectral specifications were derived from the recommendation ITU-T G.694.1 [6] on *Spectral grids for WDM applications: DWDM frequency grid*. Simulations were carried out to develop an ideal combination of materials to build a tunable, athermal, and polarization-insensitive filter whose specifications are compliant with add-drop filters in DWDM systems. A performance evaluation of the filter based on the desired specifications was performed continuously to update the model accordingly.

3. Design, analysis and simulation of the electromagnetic problem

3.1. Design and analysis of the filter

3.1.1. Through and drop port transfer functions

In DWDM communication systems, high-order Butterworth microring filters are preferred to Chebyshev filters, owing to their flat-top response [36]. Although the latter have a sharper roll-off, they exhibit ripples in the passband which put a limitation on their use especially as add-drop filters in WDM systems [19].

The order of the filter determines the number of rings in the filter. Considering the maximum attenuation of A_{max} dB in the passband and a minimum attenuation of A_{min} in the stopband, the order of the filter is given by [37]

$$n \geq \frac{log\left(\frac{10^{A_{min}/10}-1}{10^{A_{max}/10}-1}\right)}{2log\left(\frac{\omega_s}{\omega_c}\right)} \tag{1}$$

where ω_c and ω_s are the cutoff and stopband frequencies, respectively.

The transfer function of Butterworth filter is given by [37]

$$T(\omega) = \frac{1}{\left[1 + \left(\frac{j\omega}{j\omega_c}\right)^{2n}\right]^{1/2}} \tag{2}$$

According to (2), the transfer function exhibits a flat-top behavior ($T(\omega) \approx 1$) in the passband and a sharper roll-off in the stopband as the order increases.

The Coupled Mode Theory enables us to determine the transfer functions at the through and drop ports in terms of coupling coefficients. Targeting the values of $A_{max} < 1$ dB and $A_{min} > 35$ dB for DWDM systems as stipulated in [38], and using (1), the order of the filter has to be greater than five; therefore, an order of six (N = 6) has been used for the filter.

Among other ring-resonator filter configurations, the main advantage of the series-coupled microring or Coupled Resonator Optical Waveguide (CROW) filter (Fig. 1) is that a flat-top and steeper response can be realized without increasing the insertion loss [19]. Once the order of the filter is obtained, and the energy coupling formalism is used,

the transfer functions at the through and drop ports are determined by solving the coupled mode equations [34]:

$$\frac{da_1}{dt} = (j\omega_1 - \gamma_i - \gamma_0)a_1 - j\mu_1 a_2 - j\mu_0 s_i,$$

$$\frac{da_2}{dt} = (j\omega_2 - \gamma_i)a_2 - j\mu_1 a_1 - j\mu_2 a_3,$$

$$\frac{da_3}{dt} = (j\omega_3 - \gamma_i)a_3 - j\mu_3 a_1 - j\mu_3 a_4,$$

$$\frac{da_4}{dt} = (j\omega_4 - \gamma_i)a_4 - j\mu_4 a_1 - j\mu_4 a_5,$$

$$\frac{da_5}{dt} = (j\omega_5 - \gamma_i)a_5 - j\mu_4 a_4 - j\mu_5 a_6,$$

$$\frac{da_6}{dt} = (j\omega_6 - \gamma_i - \gamma_6)a_6 - j\mu_5 a_5 \tag{3}$$

Coupling between two adjacent microrings i and $i + 1$ is realized using the ring-to-ring energy coupling coefficient $\mu_i (1 \le i \le N - 1)$. In (3), the decay rate γ_i includes the intrinsic and coupling losses between the ring resonators. The decay rates γ_0 and γ_N include the intrinsic and coupling losses in the outer microrings 1 and N and the input and output straight (bus) waveguides, respectively, and can be computed as $\gamma_0 = \mu_0^2/2$ and $\gamma_N = \mu_N^2/2$.

Each microring i has resonant frequency ω_i. The wave amplitude in microring i is denoted by a_i.

The transfer functions are obtained by solving the coupled mode equations assuming the input wave excitation and the solution wave amplitudes to be harmonic, that is, $s_i \sim e^{j\omega t}$ and $a_i \sim e^{j\omega t}$, respectively.

Applying $a_i \sim e^{j\omega t}$ to Equation (3), and assuming synchronous tuning of all microrings, we get

$$(s + \gamma_0)a_1 + j\mu_1 a_2 = -j\mu_0 s_i,$$

$$j\mu_1 a_1 + sa_2 + j\mu_2 a_3 = 0,$$

$$j\mu_2 a_2 + sa_3 + j\mu_3 a_4 = 0,$$

$$j\mu_3 a_3 + sa_4 + j\mu_4 a_5 = 0,$$

$$j\mu_4 a_4 + sa_5 + j\mu_5 a_6 = 0,$$

$$j\mu_5 a_5 + (s + \gamma_6)a_6 = 0 \tag{4}$$

where $s = j(\omega - \omega_i) + \gamma_i$.

Equation (4) expressed in a matrix form, gives

$$\mathbf{X}\vec{a} = \vec{b} \tag{5}$$

where $\vec{a} = [a_1, a_2, a_3, a_4, a_5, a_6]^T$ is the solution wave amplitude array and $\vec{b} = [-j\mu s_i, 0, ..., 0, 0]^T$ is the input excitation vector, and $\mathbf{X}$ is a symmetric tridiagonal matrix:

$$\mathbf{X} = \begin{bmatrix} (s + \gamma_0) & j\mu_1 & & & & \\ j\mu_1 & s & j\mu_2 & & & \\ & j\mu_2 & s & j\mu_3 & & \\ & & j\mu_3 & s & j\mu_4 & \\ & & & j\mu_4 & s & j\mu_5 \\ & & & & j\mu_5 & (s + \gamma_6) \end{bmatrix} \tag{6}$$

The signals at the through and drop ports are related to the first and last microrings respectively by $s_t = s_i - j\mu_0 a_1$ and $s_d = -j\mu_6 a_6 s_i$. a_1 and a_6 are obtained by solving (5) using Cramer's rule,

$$a_1 = det(\mathbf{A})/det(\mathbf{X}) \qquad a_N = det(\mathbf{B})/det(\mathbf{X}) \tag{7}$$

where $\mathbf{A}$ and $\mathbf{B}$ are the matrices obtained by replacing the first and last column of $\mathbf{X}$ with $\vec{b}$ respectively. Their determinants are computed using (9) and (10)

For the tridiagonal matrix $\mathbf{X}$ given in (6), its determinant is given by $det(\mathbf{X}) = C_6(s)$, where $C_6(s)$ is the Nth-continuant obtained from the recursive formula

$$C_k = X_{6-k+1,6-k+1}C_{k-1} + \mu_{6-k+1}^2 C_{k-2} \quad , \quad k \ge 2 \tag{8}$$

with $C_0 = 1$ and $C_1 = X_{6,6}$.

$det(\mathbf{A})$ is given by

$$det(\mathbf{A}) = -j\mu_0 s_i C_5(s) \tag{9}$$

while $det(\mathbf{B})$ is given by

$$det(\mathbf{B}) = (-j\mu_0 s_i)\prod_{k=1}^{5}(-j\mu_k)$$

$$= (-j)^6(\mu_0 \mu_1 \mu_2 ... \mu_5)s_i \tag{10}$$

Equations (8) and (9) enable us to express (7) as

$$a_1 = -\mu_0 s_i \frac{C_5(s)}{C_6(s)} \tag{11}$$

Thus, using (11) and (7), we can write the through port and drop port transfer functions of the filter, respectively as

$$H_t(s) = \frac{s_t}{s_i} = 1 - \frac{j\mu_0 a_1}{s_i} = 1 - \frac{\mu_0^2 C_5(s)}{C_6(s)}$$

$$= 1 - \cfrac{\mu_0^2}{s + \gamma_0 + \cfrac{\mu_1^2}{s + \cfrac{\mu_2^2}{s + ... \cfrac{\mu_5^2}{s + \gamma_6}}}} \tag{12}$$

$$H_d(s) = \frac{s_d}{s_i} = \frac{-j\mu_6 a_6}{s_i} = \frac{(-j)^7(\mu_0 \mu_1 \mu_2 ... \mu_6)}{C_6(s)} \tag{13}$$

We can see from (12) and (13) that the transfer functions at the through and drop ports are completely determined by the coupling coefficients given in Table 1 and computed using (14) and (15).

The coupling coefficients must be properly adjusted by apodization for a finite series of microrings to mitigate the reflections of waves manifested by large ripples in the passband. Formulas for computing the energy coupling coefficients are available for Butterworth filters with a flat-top response in the passband [19]:

$$\mu_0^2 = \mu_6^2 = \frac{\Delta\omega_B/2}{sin(\pi/2 \times 6)} \tag{14}$$

$$\mu_k = \frac{(\Delta\omega/4)^2}{sin[(2k-1)\pi/2N]sin[(2k+1)\pi/2 \times 6]}, \tag{15}$$

where $1 \le k \le 5$.

The ring to bus field coupling coefficients can be deduced from the energy coupling coefficients μ_0 and μ_6 using

$$\kappa_i = \frac{\mu_i}{\sqrt{FSR}} \qquad i = 0, 6 \tag{16}$$

whereas the ring to ring field coupling coefficients are given by

$$\kappa_i = \frac{\mu_i}{FSR} \qquad 1 \le i \le 5 \tag{17}$$

3.1.2. Material system and physical parameters determination

As mentioned in Section 1, alternative materials to the $Si - SiO_2$ material system should be investigated to mitigate the intrinsic weaknesses of Si, especially its thermal sensitivity of the optical index, poor electro-optic coefficients and indirect band-gap despite its high index contrast, low loss, and CMOS compatibility [39]. Therefore, an appropriate waveguide engineering must be done to avoid thermal fluctuations of the resonant wavelength and for the filter to accommodate arbitrarily polarized signals, while minimizing the polarization rotation, and thermal sensitivity, and still have CMOS compatibility and small size. In addition, the material system should allow the filter to be tunable with low power consumption.

We first examine the temperature-dependent wavelength shift (TDWS) [40]:

$$\frac{d\lambda}{dT} = \frac{\lambda}{n_g} \left(\frac{\partial n_{eff}}{\partial T} + n_{eff}\alpha \right) \tag{18}$$

where n_g is the group index of the waveguide and α the coefficient of thermal expansion (CTE). Local heating and environmental temperature variation are responsible for the variation in the effective index and the group index (thermo-optic effects) and the expansion in the perimeter of the rings (thermo-elastic effects). From (18), the TDWS is seen as a combination of thermo-optic and thermo-elastic effects. The TDWS can be estimated by calculating the effective index of the waveguide as a function of temperature. We assume that the effective index (20)-(21) does not depend on the wavelength because we are interested in a small range of wavelengths around the resonant wavelength. The influence of CTE on TDWS is negligibly weak compared to the thermo-optic coefficient (TOC) for Silicon photonic wavelength filters [40] and will be omitted ($\alpha \approx 0$), i.e.,

$$\frac{d\lambda}{dT} \approx \frac{\lambda}{n_g} \left(\frac{\partial n_{eff}}{\partial T} \right). \tag{19}$$

The effective index of the waveguide is given by

$$n_{eff} = \Gamma_{core}n_{core} + \Gamma_{clad}n_{clad} \tag{20}$$

where Γ_{core} and Γ_{clad} are the confinement factors in core, and cladding, respectively.

Therefore, we reduce the TDWS by adjusting the temperature dependence of the effective index, that is, using two different materials for the under-cladding and upper-cladding.

$$n_{eff} = \Gamma_{core}n_{core} + \Gamma_{up}n_{up} + \Gamma_{un}n_{un} \tag{21}$$

Γ_{up} and Γ_{un} are the under-cladding, and upper-cladding confinement factors, respectively.

$$\frac{\partial n_{eff}}{\partial T} \approx \Gamma_{core}\frac{\partial n_{core}}{\partial T} + \Gamma_{up}\frac{\partial n_{up}}{\partial T} + \Gamma_{un}\frac{\partial n_{un}}{\partial T} \tag{22}$$

If we choose to use silicon oxide (SiO_2) as the undercladding material, its thermo-optic coefficient is quite low ($2.6 \times 10^{-6}/K$), thus can be neglected.

The condition of athermal operation (zero TDWS condition) of the waveguide is then given by

$$\frac{\partial n_{eff}}{\partial T} \approx \Gamma_{core}\frac{\partial n_{core}}{\partial T} + \Gamma_{up}\frac{\partial n_{up}}{\partial T} \approx 0 \tag{23}$$

or

$$\Gamma_{core}\frac{\partial n_{core}}{\partial T} \approx -\Gamma_{up}\frac{\partial n_{up}}{\partial T} \tag{24}$$

The idea in this work is to use different materials for under-cladding and upper-cladding where the core and upper-cladding materials have thermo-optic coefficients with opposite signs to design a device with an athermal behavior.

To make the designed waveguide polarization-insensitive, the waveguide should only support fundamental quasi-TE and quasi-TM modes, and its birefringence should be zero, that is, the effective indices of the TE and TM fundamental modes should be the same ($n_{eff,TE} = n_{eff,TM}$). In addition, the coupling efficiencies should be the same for both polarizations ($\kappa_{TE} = \kappa_{TM}$).

When the bending radius is further reduced, in addition to increasing losses, the induced stress enhances the birefringence in the waveguides. A critical radius was determined during the mode analysis. The general linear stress-optical relation can be written, using tensor notation, as follows:

$$\Delta n_{ij} = -B_{ijkl}S_{kl} \tag{25}$$

where $\Delta n_{ij} = n_{ij} - n_0I_{ij}$, n_{ij} is the refractive index tensor, n_0 is the refractive index of a stress-free material, I_{ij} is the identity tensor, B_{ijkl} is the stress-optical tensor, and S_{kl} is the stress tensor. In this study, the

structure is free to bend in the y direction. A mode solver was used to determine the critical bending radius that minimizes polarization rotation.

To develop a polarization-insensitive and an athermal device, an appropriate choice of waveguide materials, and an adjustment of the aspect ratio of the cross-section dimensions of the waveguides have been made. The waveguide mode analysis of the chosen cross-section of the waveguide allowed us to evaluate the field confinement ratios, effective, and group indices in the fundamental TE and TM modes as shown in Fig. 7.

Thus, to realize an athermal and polarization-insensitive waveguide, a material system integrated on top of a silicon substrate, composed of silicon oxide -silicon rich nitride-titanium oxide ($SiO_2 - Si_3N_4 - TiO_2$) as the under-cladding, core and upper-cladding materials respectively has been used. This material system is CMOS-compatible, thus, the device can be integrated on a Si-photonics platform, enabling low-power dense wave division multiplexing (DWDM) solutions. An additional interesting feature of this material system is the higher electro-optic coefficient of Si_3N_4 compared to silicon which leads to the demonstration of electro-optical effects [41] enhanced by placing a thin-layer of lithium niobate as mentioned in Subsection 3.4. For fabrication considerations, a process was investigated and suggested for this model. Due to its compatibility with silicon photonics platforms, silicon-rich nitride can be directly deposited by plasma-enhanced chemical vapor deposition (PECVD) on a thin film of lithium niobate [42]. The layer of lithium niobate is bonded to a PECVD-deposited silicon oxide on a silicon substrate. The titanium dioxide layer is deposited by low temperature sputtering, which allows the deposition of a very smooth TiO_2 layer [32], experimentally proved in [43]. Replacing silicon with silicon-rich nitride (Si_3N_4) with a low index contrast, simultaneously reduces the difference in the coupling efficiencies for both polarizations. Titanium oxide was chosen for its negative TOC and its insensitivity to humidity as compared to polymers [33]. The material system is simultaneously athermal, polarization-insensitive, CMOS-compatible, and electro-optically tunable.

3.2. Waveguide mode analysis

During this step, the shape and optical properties of the waveguide have to enable strong confinement of quasi-all the energy of the fields (for both polarizations) in the core section of the waveguide.

The dimensions of the cross-section, the radius (R) of the ring resonator; the straight waveguide length greater than the beat length, L_B (29), the gap distances between the waveguide and ring resonators and inter-ring gap distances are determined during the waveguide mode analysis step thus enabling to relate the spectral parameters to the physical and optical properties of the filter. In particular, the dimensions were chosen to allow single mode operation. A critical radius is determined to minimize bending losses and mitigate polarization rotation. Parameters such as effective refractive index n_{eff}, group index n_g, fundamental mode confinement factor, Free Spectral Range ($FSR \sim 1/R$), Full Wave Half Maximum ($FWHM \sim 1/R$), loaded Q-factor ($Q \sim R$) depend directly on the waveguide dimension and the materials properties.

The FSR is linked to the group index and the ring radius by

$$FSR = \frac{c}{n_g 2\pi R} \tag{26}$$

where c, R, and n_g are the speed of light in free space, ring radius, and group index, respectively.

From (14), (15), (16), and (17), the coefficients required for a flat-top response can be determined for a given bandwidth of the filter. The following coupling equation allows us to deduce different gap distances from the corresponding field coupling coefficients using [44];

$$\kappa = sin(\frac{\pi}{\lambda}[\frac{a_E}{\gamma_E}e^{-\gamma_E d}B(x_E) + \frac{a_O}{\gamma_O}e^{-\gamma_O d}B(x_O)]) \tag{27}$$

where $B(x_E)$, $B(x_O)$, n_E, and n_O are the curvature functions and effective indices for the odd, and even supermodes, respectively. a_E, a_O γ_E and γ_O in (27) are determined from

$$n_E = n_{eff} + a_E e^{-\gamma_E d} \qquad n_O = n_{eff} - a_O e^{-\gamma_O d} \qquad (28)$$

for different values of gap distance d. The lower boundary of the straight waveguide length L_s is fixed by the beat length

$$L_s > L_B = \lambda_0 \frac{(n_E - n_O)}{2} \qquad (29)$$

The results of the mode analysis are shown in Figs. 7 and 8.

3.3. 3D simulation of the filter

The computational domain can be significantly reduced for the simulation of the device structure. In fact, the energy of the fundamental modes is concentrated in the core region and the energy density decays exponentially in the cladding and buffer regions, it is not necessary to model the air and substrate domains.

This model computes the propagation of light (electromagnetic waves) in the filter. Optical signal in TE/TM mode applied to the input port with wavelengths satisfying the resonance condition, that is, $m\lambda_{res} = 2\pi R n_{eff}$, where m is an integer, and n_{eff} is the effective index of the microring waveguide was transmitted at the drop port at different temperatures. S-parameters measured at through and drop ports gave the transfer functions at the related ports. Electro-optical tuning and parameter adjustment were performed to obtain the characteristics of the filter in compliance with the targeted specifications for add-drop filters in DWDM systems.

The inherent properties of optical waveguides such as bounded propagated fields (total internal reflection), known propagation directions, waveguide length compared to the signal wavelength, and finally waveguides bent sections (not always straight) enable us to choose Finite Element Method, Electromagnetic Waves Beam Envelope (FEM-EWBE) propagation method for this step. This method facilitates the reformulation of the Helmholtz equation (30) without any approximations to overcome some simulation challenges especially the reduction of the number of mesh elements that will be required and thus develop an economic model in terms of computer resources and simulation time [45].

The FEM-EWBE propagation method solves the Maxwell wave equation in the frequency domain (stationary problems) which are reduced to the Helmholtz equation:

$$\nabla \times \mu_r^{-1}(\nabla \times \vec{E}) - k_0^2(\epsilon_r - \frac{j\sigma}{\omega\epsilon_0})\vec{E} = 0 \qquad (30)$$

For this method, we replace the electric field with its phasor form in the standard Helmholtz equation:

$$\vec{E} = \vec{E} exp(-i\vec{k}.\vec{r}) \qquad (31)$$

where $\vec{k}$, the wave vector is computed using (37).

The field is factored into the product of slowly varying envelope of the field $\vec{E}$ and an average phase variation over the distance traveled by the field given by the wave vector $\vec{k}$ [45]. This leads to the following partial differential equation (PDE):

$$(\nabla \times i\vec{k}) \times \mu_r^{-1}((\nabla - i\vec{k}) \times \vec{E}) - k_0^2(\epsilon_r - \frac{j\sigma}{\omega\epsilon_0})\vec{E} = 0 \qquad (32)$$

Equations (33), (34), (35), and (36) enable us to consider the following boundary conditions:

1. The tangential components of the E-field (31) and H-field are zero at the inner boundaries of the ring resonators (perfectly absorbing boundaries)

$$\vec{n} \times \vec{E} = \vec{0} \qquad \vec{n}.\vec{H} = \vec{0} \qquad (33)$$

2. The outer boundaries are made transparent to the outgoing waves by applying the scattering boundary condition:

$$\vec{n} \times \nabla \times \vec{E} - (ik)\vec{n} \times \vec{E} \times \vec{n} = \vec{0} \qquad (34)$$

where $k = 2\pi/\lambda$, the wave number.

3. The excitation source was set at the input port, whereas the drop and through ports were set off:

$$\vec{n} \times \nabla \times \vec{E} - i\beta\vec{n} \times \vec{E} \times \vec{n} = \vec{0} \qquad (35)$$

4. The tangential components of the electric/magnetic fields are continuous at the boundaries between waveguides for field continuity,

$$\vec{E}_{T,1} = \vec{E}_{T,2} \qquad \vec{H}_{T,1} = \vec{H}_{T,2} \qquad (36)$$

The key to successful resolution of the Helmholtz equation using the beam envelope propagation method is the proper definition of the wave vector $\vec{k} = (k, 0)$ or equivalently the phase function $\phi = \vec{k}.\vec{r}$, where $\vec{r}$, is the position vector.

k is the longitudinal propagation constant, which can also be written as $k_\parallel$, and is related to the transverse propagation constant as follows:

$$\vec{k} = \vec{k}_\parallel + \vec{k}_\perp \qquad (37)$$

$\vec{k}_\perp$ corresponds to the boundary mode which is the transverse component of the field $\vec{E}_T$. The transverse propagation constant $k_\perp$ is calculated during the boundary mode analysis. The longitudinal propagation constant, $k_\parallel$, was computed analytically from

$$k^2 = n^2\omega^2 c^2 = k_\parallel^2 + k_\perp^2 \qquad (38)$$

The longitudinal constant can deviate due to different factors. The deviation of the propagation constant (38) is mostly due to the perturbation of the cross-section from the original rectangular form or due to different layers of the material system [46]. The field continuity boundary condition (36) applied at the limits of straight and ring waveguides reduces significantly this difference. Another source of propagation constant deviation is related to the change of the effective index ($\Delta k_\parallel = \Delta n_{eff} 2\pi/\lambda$).

3.4. Free spectral range extension and electro-optic tuning

To increase the tuning range of the filter, microrings of different radii can be used to exploit the Vernier effect (Fig. 2). The resulting device exhibited resonance only, where the individual resonances of all involved microrings match and thus extend the FSR. The extended FSR is related to the FSR of each ring as follows;

$$FSR_{extended} = m_1 FSR_1 = m_2 FSR_2 \qquad (39)$$

where m_1 and m_2 are integers.

While the signal propagates through the filter, the ring resonant wavelength slightly deviates from the center wavelength. This results in a deviation of the center wavelength of the filter from the design wavelength. To make the filter wavelength tunable, the filter's center wavelength can be shifted to different values proposed in the grid for DWDM systems [6]. In this work, the linear electro-optic effect (Pockels effect) is used to control the optical properties with an externally applied drive voltage where the refractive index changes proportionally with the applied voltage. The change in the refractive index enabled us to adjust the filtered wavelengths. The Electro-optic (EO) effect can be enhanced by deposition of a thin-film of Lithium Niobate with a high EO coefficient (33 pm/V) [47] on top of the silicon dioxide and hence reduce the applied voltage (low power consumption). This association has been used in high-speed electro-optic modulators [42][48][49] operating at low voltages. Graphene electrodes are preferred to conventional metal electrodes to prevent the need of buffer layer and further reduce the drive voltage [50].
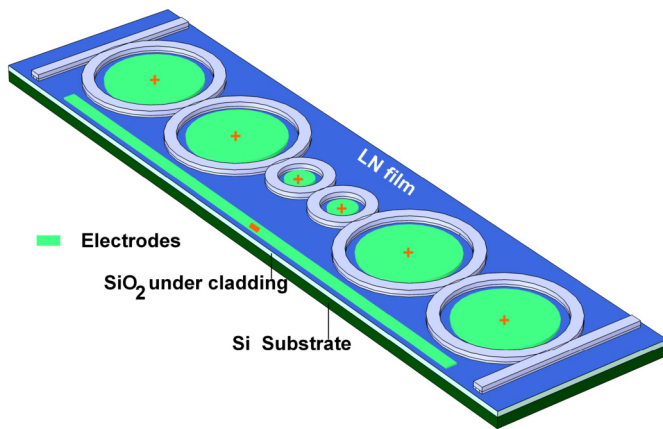
Fig. 2. Proposed 3D filter Model design. A thin film of the lithium niobate (shown as LN) is placed on the top of the undercladding material (under the core material).
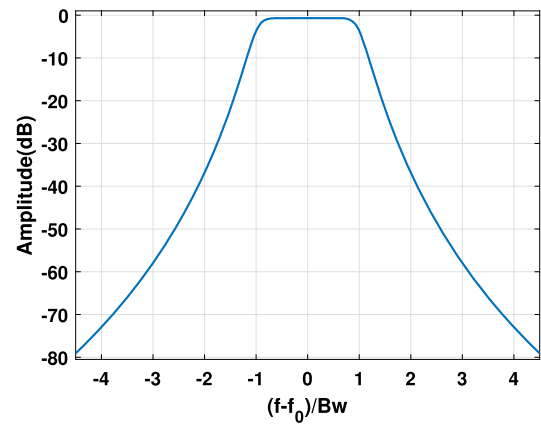

Fig. 4. A sixth-order Butterworth filter with $A_{max} = 0.7$ dB, $A_{min} = 36$ dB, $w_{cnorm} = 1$, $w_{snorm} = 2$.
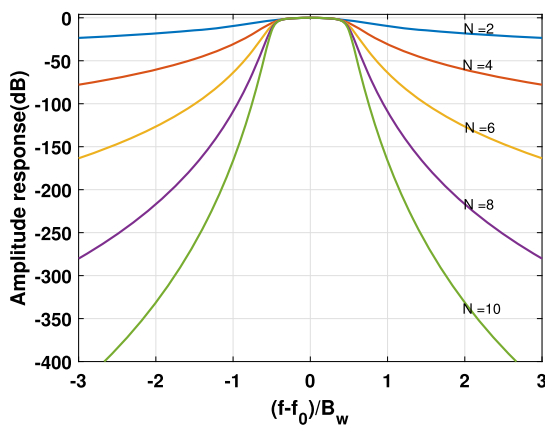

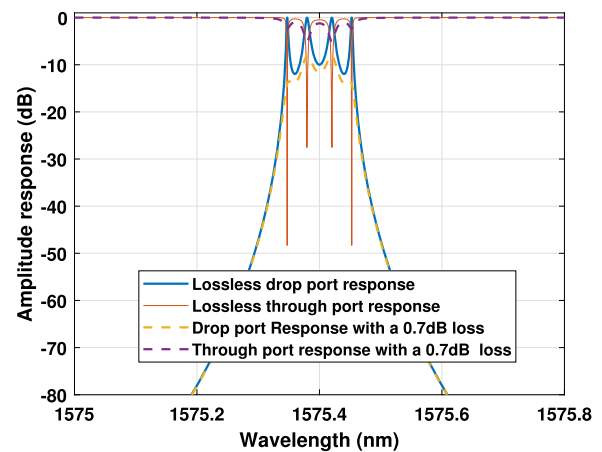**Fig. 3.** Magnitude of normalized band-pass Butterworth filters as the order increases.

Fig. 5. Transfer functions without coupling coefficients apodization. The finite length of the rings series results in ripples caused by the reflections at the terminations.

4. Results and discussions

Fig. 3 shows the theoretical flat-top spectrum responses of Butterworth filters as the order increases. From (2), it can be clearly seen that higher-order Butterworth filters can achieve a flat-top filter response in the passband (H(ω) ≈ 1 or ≈ 0 dB) and a steeper roll-off in the stopband.

Similarly, the shape factor (SF) increases with the order of the filter. The higher the order, the higher the shape factor or the smaller cross-talk with neighboring channels. The filter's response of a sixth-order Butterworth filter (Fig. 4) is much flat-top and steeper than the lower-order filters and exhibits an SF of 0.74, an obvious improvement compared to the first order case (SF = 0.17).

In this study, a maximum attenuation in the passband of 1 dB and a minimum attenuation of 35 dB in the stopband were targeted. Fig. 4 shows that a sixth-order Butterworth filter this target has been successfully achieved.

Using the topology shown in Fig. 1, a six-ring resonator-based add-drop filter was designed by solving the coupled mode equations. The results are presented in Figs. 5 and 6. The drop port and through port responses are presented for a sixth-order serially coupled microring filter with a 3 dB Full Wave Half Maximum (FWHM) bandwidth of 50 GHz (0.4 nm) with a center wavelength of $\lambda_0 = 1575.4$ nm in the L-band. In this process, the choice of coupling coefficients is of a paramount importance. In fact, due to the finite length of the series of rings of the filter, large ripples appear in the passband of filter's drop response as illustrated in Fig. 5. This can be prevented by a proper adjustment (or apodization) of the coupling coefficients. The apodized coefficients ex-

Table 1. Apodized energy coupling coefficients ($\mu(i)$) and field ($\kappa(i)$) coupling coefficients of a 50 GHz-bandwidth and 517 GHz-FSR sixth-order filter.

i	$\mu(i)$ [GHz$^{1/2}$]	$\kappa(i)$
0	12.3178	0.541628817
1	45.8975	0.088741397
2	23.7583	0.045935938
3	20.3276	0.039302786
4	23.7583	0.045935938
5	45.8975	0.088741397
6	12.3178	0.541628817

hibit symmetry ($\mu_0 = \mu_N$, $\mu_i = \mu_{N-i}$ or $\kappa_0 = \kappa_N$, $\kappa_i = \kappa_{N-i}$, $1 \leq i \leq N-1$) as assessed by the computed values in Table 1 according to (14) and (15). This leads to a more optimized filter with a maximally flat response and a steeper roll-off factor of 35 dB, in compliance with the targeted application, as shown in Fig. 6. In the same graph, it is shown that when the microrings are considered as a lossy medium, the transmission response is less than unity (0 dB) for the drop port response and a less pronounced notch behavior of the through port response in the passband is observed (Fig. 6).

The Coupled Mode Theory (CMT) does not relate spectral properties to the physical and optical properties of the filter. To achieve this, a waveguide mode analysis is performed on the chosen material system for the filter. From this analysis, an athermal and polarization-
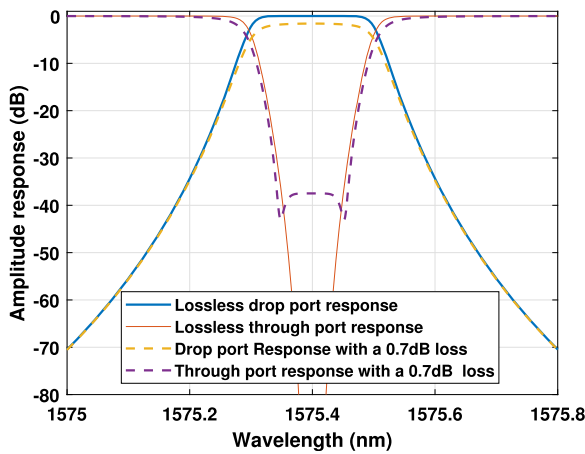
Fig. 6. Drop and Through ports amplitude responses of a 50 GHz-bandwidth sixth-Order ring resonator-based filter.
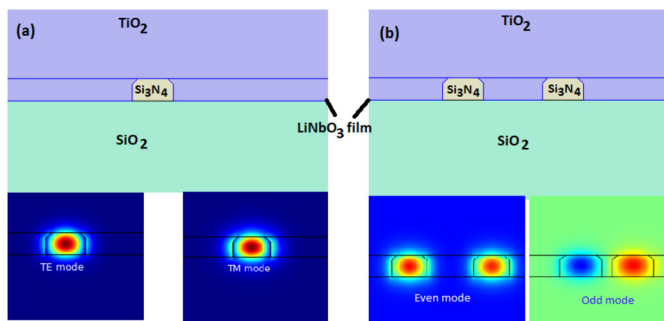

Fig. 7. Titanium oxide (TiO_2), silicon-rich nitride (S_3N_4), and silicon oxide (SiO_2) were used as the upper-cladding, core, and under-cladding materials, respectively. (a) Top: Uncoupled waveguide cross-section. Bottom: TE and TM fundamental modes. (b) Top: Coupled waveguide cross-sections. Bottom: Super-modes (even and odd modes). Their effective indices are given by (28).

insensitive waveguide was designed. To keep the fields well confined in the waveguide for a single mode operation, a 670×375 nm modified (chamfered) rectangular cross-section was used with as chamfer height of 75 nm at an angle of 45° (Fig. 7). A critical ring radius of 36 μm allowing minimal bending losses (6.32×10^{-5} dB/cm) and preventing polarization rotation was determined using a mode solver. The effective indices for the TE and TM fundamental modes are 2.018872 and 2.018871 whereas the group indices are 2.564343, and 2.564341, respectively, which are very close in both polarizations. The field confinement factors for the TE and TM fundamental modes are $\Gamma_{TE} = 98.3\%$ and $\Gamma_{TE} = 97.5\%$ respectively. We observed a high confinement of the field energy in the core of the waveguide because of the careful choice of waveguide parameters. The boundary mode analyses performed on through and drop ports result in a deviation of the longitudinal propagation constant of 3.6126×10^{-6} rad/m. This slight deviation is explained by a proper definition of the propagation constant in straight and ring resonators and the application of the field continuity boundary condition at their intersection.

From the results of the mode analysis, the apodized coupling coefficients, and using (27), the gap distances were determined. The symmetry found in the coupling coefficients was also observed for the corresponding gap distances (Fig. 8).

The results of the 3D multiphysics study from solving the electromagnetic problem (32) in the geometry of the filter using the FEM-EWBE propagation method are presented (Figs. 9-22). The electric field profile in the filter at resonance is shown in Fig. 9. This shows strong coupling of the fields in the ring resonators.
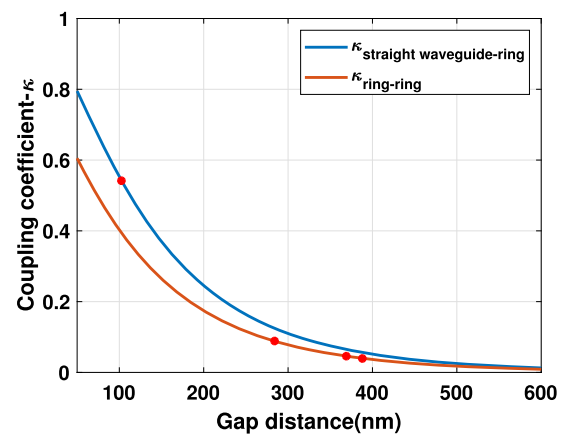

Fig. 8. Coupling coefficient vs the coupling gap distance according (27). The red dots in the graph show gap distances (d_i) and the corresponding coupling coefficients used for the model. $d_0 = d_6 = 102.5$ nm, $d_1 = d_5 = 284$ nm, $d_2 = d_4 = 369$ nm and $d_3 = 388$ nm.
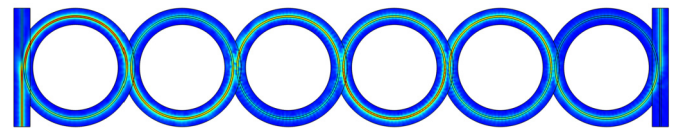

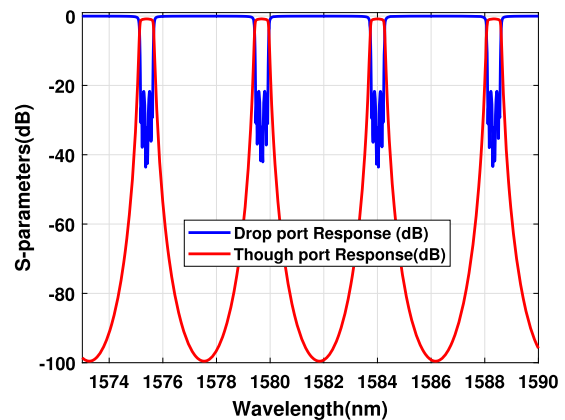**Fig. 9.** xy-plane view of the Electric field profile in the TE mode.

Fig. 10. Six ring resonator-based filter transfer functions at drop and through ports at $T = 298$ K in TE mode. Loss $= 0.82$ dB, $B_w = 50$ GHz (0.4 nm) with FSR $= 517.6$ GHz, and an extinction ratio (ER) $= 98$ dB.

The S-parameters measured at the through and drop ports respectively provide the transfer functions on the related ports, as presented in Fig. 10. We observed a flat-top drop port response in the passband. The filter characteristics from the simulation at $T = 298$ K in TE mode (TM mode giving practically the same profile) are as follows: loss $= 0.82$ dB, $B_w = 50$ GHz (0.4 nm) around the center wavelength of 1575.5 nm, FSR $= 517.6$ GHz (in accordance with (26)), Q $= 3207$, Finesse $= 8.79$ and an extinction ratio (ER) $= 98$ dB.

These results (Fig. 10) meet the targeted characteristics of the filter. However, the FSR has to be expounded for the filter to accommodate more channels without interference. This can be extended using different radii for the ring resonators (Vernier effect) as shown in the proposed geometry (Fig. 2) and the electric field profile is given in Fig. 11.

The resulting FSR and finesse are 2.537 THz and 31, respectively. Owing to Vernier effects, this filter can accommodate five times more channels (Figs. 12, 11, and 20) and can be extended further to allow the filter to be tuned over the full range of the L-band.
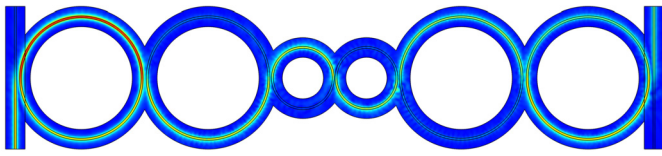
Fig. 11. xy-plane view of the electric field profile in the TM mode for FSR extension (Vernier effect). $r_1 = r_2 = r_5 = r_6 = 36\,\mu m$, $r_3 = r_4 = 7.2\,\mu m$ at $T = 298K$.
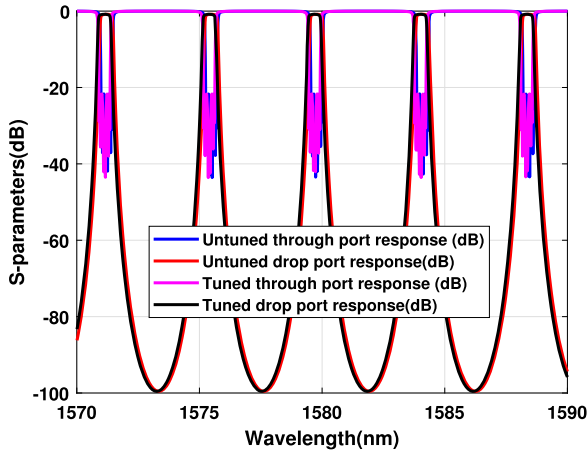

Fig. 12. Electro-optically tuned Drop and Through Responses, $B_w = 0.4$ nm.
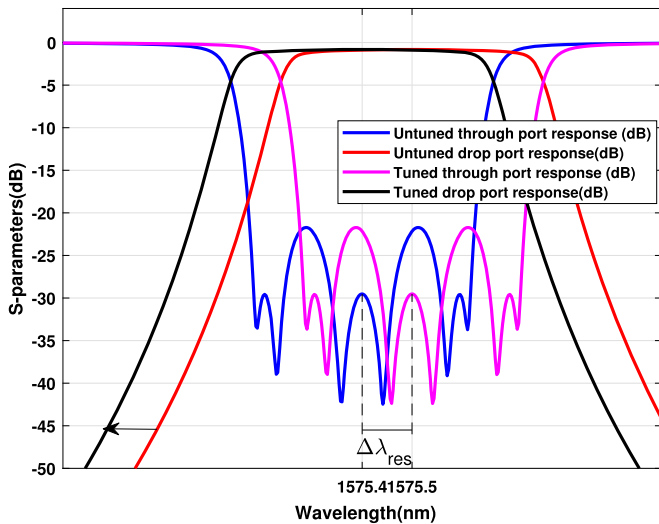

Fig. 13. Magnified view of the tuning process. The resonant wavelength is electro-optically tuned from 1575.5 nm to 1575.4 nm.

To adjust the resonant wavelength to the design wavelength (1575.4 nm), a DC voltage of 11 V was applied through the electrostatics physics added to the model. The potential profile in the electrodes is illustrated in Fig. 15. The resonant wavelength was adjusted using a parameter sweep of the applied voltage. A magnified view of Fig. 12 around the first resonance is shown in Fig. 13 to provide a clear picture of the tuning process. The gap between the TiO_2 upper-cladding and the graphene electrodes applied on the lithium niobate thin film was set to 2 μm close enough to excite the EO effect in the waveguide and sufficiently far to avoid additional losses (Fig. 2). The filter can achieve a high tuning efficiency of 8.95 pm/V (Fig. 14 and 16).

Uniform ambient temperature variations and a non-uniform thermal excursion from the substrate are incorporated. The temperature distribution is shown in Fig. 17. These variations may result in additional variation in the effective and the group indices (thermo-optic effects)
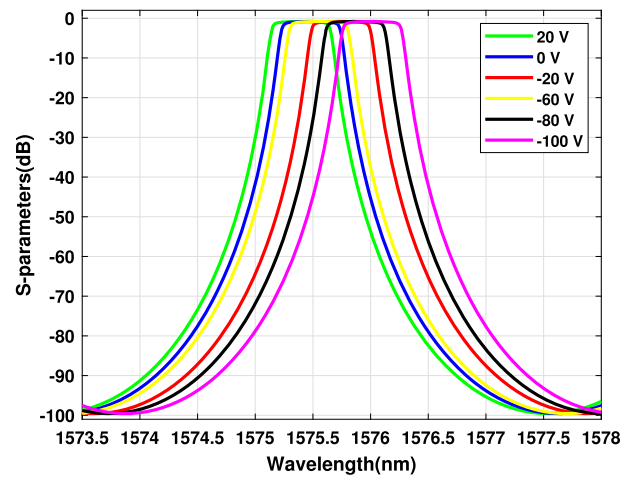

Fig. 14. The center wavelength shift of the filter originally at 1575.5 nm (blue curve) as a function of the applied voltage; Applied voltage varies from -100 V to 100 V. The measured tunability is 8.95 pm/V.
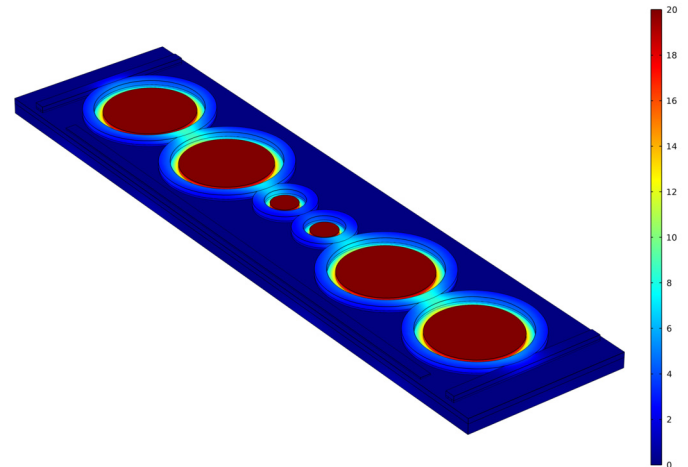

Fig. 15. Potential profile in electrodes. The microrings are tuned synchronously by placing electrodes in the center of each microring.
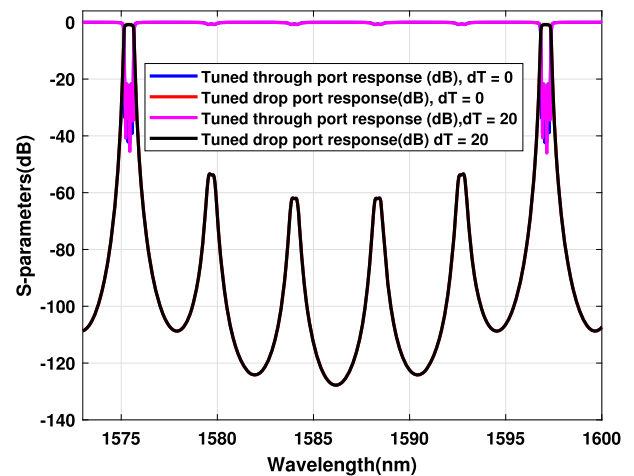

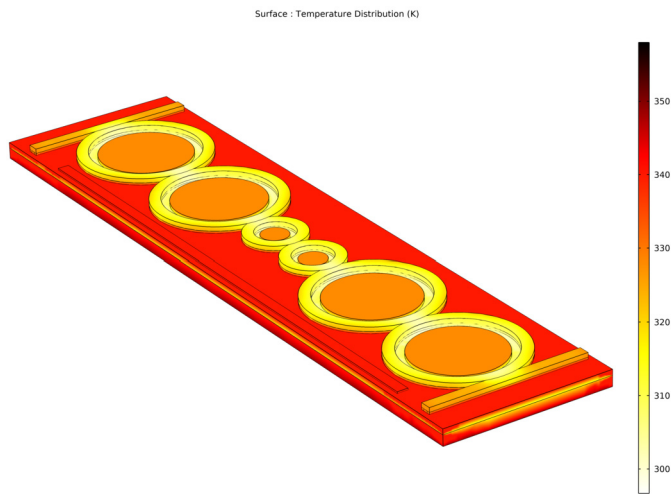**Fig. 16.** Data on the resonant wavelength shift as a function of the applied DC voltage with a linear fitting.
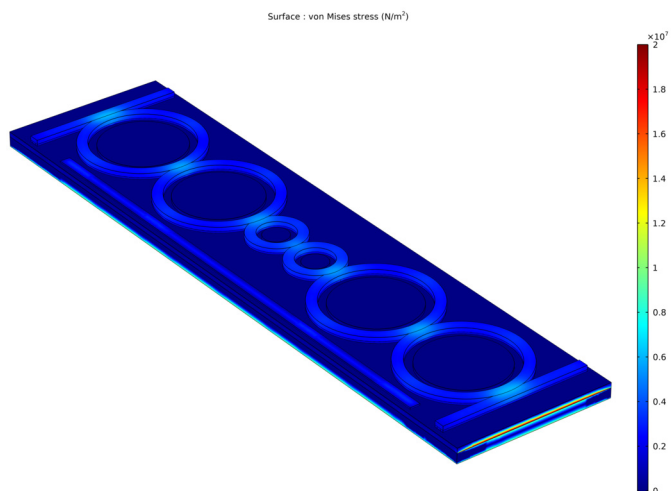
Fig. 18. von Mises stress distribution in the filter as ambient temperature changes from 298 K to 318 K in the study, with local heating from the bottom of the substrate of 60 K.

Fig. 19. Temperature sensitivity of the TE mode as the temperature changes from 298 K to 318 K, with extended FSR (Vernier effect).

Fig. 20. Temperature sensitivity of the TM mode from 298 K to 318 K, with extended FSR (Vernier effect).

and the expansivity of the microrings (stress-optical effects) as given in (25) and therefore detune the filter resonance.

The von Mises stress distribution is given in Fig. 18. For both temperature and stress distributions, their effects on the filter are negligible except for a slight increase of values in the joints of different layers mainly due to mismatches of coefficients of thermal expansions between the substrate and the silicon dioxide layers. However, this effect is not observed at the interface between silicon oxide and silicon-rich nitride layers due to the low coefficient of thermal expansion of silicon oxide as assumed in (19). At $T_0 = 298$ K, the center wavelength is practically the same for both the TE and TM modes. When the temperature is increased in the structure of the filter (Fig. 17) from 298 K ($dT = 0$) to 318 K ($dT = 20$), there is quite a perfect overlap of the graphs for the TE mode (Fig. 19) and a slight shift in the center wavelength from 1575.437 nm to 1575.448 nm for TM mode (Fig. 20). Additionally, an increase of loss in the passband (1.32 dB) was observed for the TM mode. This shows the athermal behavior for both modes. The slight shift (11 pm of 0.5 pm/K) in the TM mode is due to the fact that the TDWS zero condition (23) or (24) used the TE mode parameters but did not alter the performance of the targeted application. The difference in the loss is mainly due to the difference in the absorption of the two modes in the device material, and the difference in bending losses for the two modes. These results also confirm the optimal adaptation of the materials, the
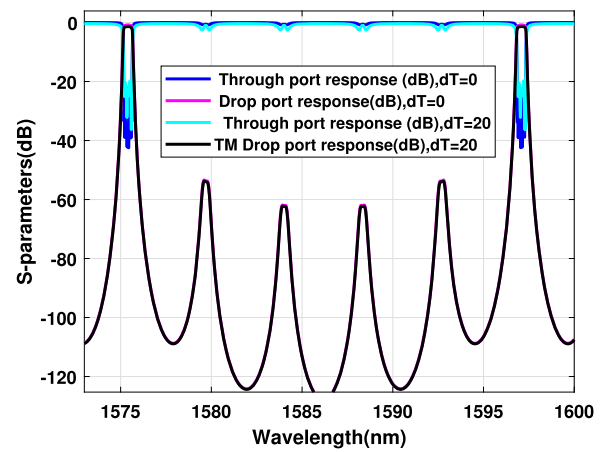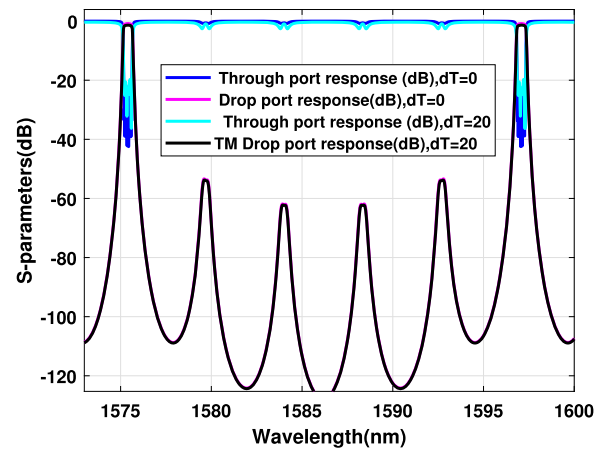
cross-section of the waveguides, and the critical radius in the microrings. Additionally, the choice of the location of the electrodes as well as the thickness of the lithium niobate layer were carefully done to avoid additional losses and did not affect the athermal and polarization independence behavior of the filter.

In comparison, the $SiO_2 - Si - SiO_2$ material system exhibits lower losses (0.69 dB) in the TE mode, a smaller footprint (for a 450 nm × 220 nm rectangular cross-section of the waveguide and a ring radius of 7.2 nm), and a larger FSR but is thermally unstable ($d\lambda_{res} = 85$ pm/K). Additionally, the performance in the TM mode was not conclusive. An attempt to reduce the temperature sensitivity by replacing SiO_2 with TiO_2 as an upper-cladding material has also been investigated. The device exhibited higher losses (0.77 dB) but has a much better temperature stability ($d\lambda_{res} = 2.5$ pm/K). Furthermore, by replacing silicon by tantalum pentoxide (Ta_2O_5) as a core material, much better thermal stability compared with Si-based waveguide devices was achieved ($d\lambda_{res} = 1.32$ pm/K) at the expense of the size of the device. Attempts to obtain polarization-insensitive devices with these material systems have not been successful. Our selected material system exhibited better performance for TE and TM modes with resonant wavelength stability, $d\lambda_{res} < 0.2$ pm/K for TE mode and $d\lambda_{res} < 0.5$ pm/K for TM mode (Fig. 21). Additionally, with the choice of a critical bending radius and a multi-material system that minimizes stress-optical effects (Fig. 18) in the filter, and thermo-optic effects as expressed by (22), the device showed good stability of the refractive index versus temperature
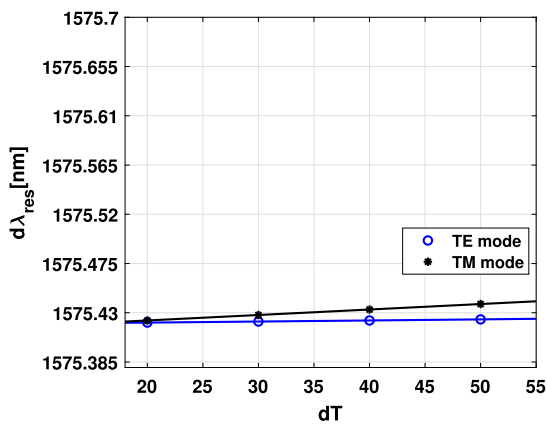
Fig. 21. Dependence of the center wavelength to the temperature variation.
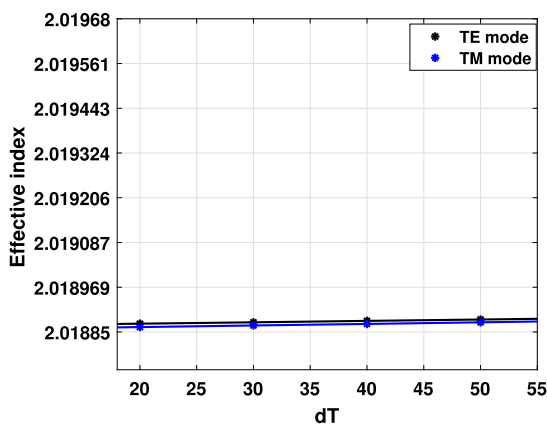

Fig. 22. Effective index vs temperature. The graph shows no dependence of the effective index on the temperature, confirming the compensation of the thermo-optic effects predicted earlier in (22) by the design.

variation (Fig. 22). This validates the assumptions made in ((19) and (23)).

5. Conclusion

This work focused on designing and analyzing a tunable, athermal, and polarization-insensitive add-drop optical filter based on ring resonators for DWDM systems. The objective was to determine the physical and optical parameters of the filter that met the spectral specifications imposed by DWDM systems. Accordingly, a 3D multiphysics approach was used on a carefully chosen material system. The results demonstrate an innovative tunable filter that can be used with arbitrarily polarized signals with high thermal stability and an extended FSR which can be further extended to cover the full range of the L-band.

The future goal of this research will be to consider other tuning methods such as all-optical tuning methods and hence compare the performance with the electro-optical method used in the work in terms of speed, power consumption, and range.

Declarations

Author contribution statement

Filston Rukerandanga: Contributed reagents, materials, analysis tools or data; Analyzed and interpreted the data; Contributed reagents, materials, analysis tools or data; Wrote the paper.

Stephen Musyoki: Contributed reagents, materials, analysis tools or data.

Edwin Omondi Ataro: Analyzed and interpreted the data; contributed reagents, materials, analysis tools or data.

Data availability statement

No data was used for the research described in the article.

Declaration of interests statement

The authors declare no conflict of interest.

Additional information

No additional information is available for this paper.

References

[1] A.E. Willner, A. Fallahpour, F. Alishahi, Y. Cao, A. Mohajerin-Ariaei, A. Almaiman, P. Liao, K. Zou, A.N. Willner, M. Tur, All-optical signal processing techniques for flexible networks, J. Lightwave Technol. 37 (1) (2019) 21–35.

[2] S. Pato, Capacity increase and hardware savings in DWDM networks exploiting next-generation optical line interfaces, in: 2018 20th International Conference on Transparent Optical Networks (ICTON), 2018, pp. 1–6.

[3] Lovkesh, R. Kaur, Estimation of four wave mixing effect in pre-, post- and in-line configuration of EDFA using advanced modulation formats for 1.28 Tbps WDM system, Opt. Quantum Electron. 53 (2021) 194.

[4] S. Li, W. Chen, P. Wang, Q. Fu, J. Zhang, B. Zhang, T. Dai, Y. Wang, J. Yang, Bandwidth-tunable optical passband filter based on graphene-silicon waveguide, Opt. Commun. 426 (December 2017) (2018) 206–211.

[5] S. Bélanger-de Villers, D. Hould, W. Shi, Ultra-compact DWDM filter tunable across the C-band, in: Optical Fiber Communication Conference, Optical Society of America, 2019, W2A–4.

[6] ITU-T, G.694.1. Spectral grids for WDM applications: DWDM frequency grid, Ser. G.694.1, Feb. 2012, pp. 1–16, https://www.itu.int/rec/T-REC-G.694.1-201202-S/en.

[7] H. Wang, J. Dai, H. Jia, S. Shao, X. Fu, L. Zhang, L. Yang, Polarization-independent tunable optical filter with variable bandwidth based on silicon-on-insulator waveguides, Nanophotonics 7 (2018) 1469–1477.

[8] Y. Liu, Z. Li, D. Li, Y. Yao, J. Du, Z. He, K. Xu, Thermo-optic tunable silicon arrayed waveguide grating at 2-μm wavelength band, IEEE Photonics J. 12 (4) (2020) 1–8.

[9] Y. Yang, R. Lu, L. Gao, S. Gong, 4.5 GHz lithium niobate MEMS filters with 10 fractional bandwidth for 5G front-ends, J. Microelectromech. Syst. 28 (4) (2019) 575–577.

[10] E. Ataro, Micro-Electromechanical Structural Design and Optimization of Vertical Cavity Photonic Devices with Wide Continuous Tuning, Verlag nicht ermittelbar, 2005, https://books.google.co.ke/books?id=gWQlPQAACAAJ.

[11] C. Kim, W.-B. Lee, S.K. Lee, Y.T. Lee, H.-N. Lee, Fabrication of 2D thin-film filter-array for compressive sensing spectroscopy, Opt. Lasers Eng. 115 (2019) 53–58, https://www.sciencedirect.com/science/article/pii/S0143816618302379.

[12] M. Kamran, K. Abedi, M.J. Sharifi, Novel multi-stage photonic crystal Mach-Zehnder optical filters, IEEE Photonics Technol. Lett. 30 (21) (2018) 1874–1877.

[13] K. Zhang, Y.-A. Peter, M. Rochette, Chalcogenide Fabry–Perot fiber tunable filter, IEEE Photonics Technol. Lett. 30 (23) (2018) 2013–2016.

[14] D. Chadha, Optical WDM Networks: From Static to Elastic Networks, Wiley, 2019, arXiv:1011.1669v3.

[15] H. Venghaus, Wavelength Filters in Fibre Optics, Springer Series in Optical Sciences, 2007.

[16] S. Song, S.X. Chew, X. Yi, L. Nguyen, R. Minasian, Tunable single passband microwave photonic filter using a cascaded pair of microring resonators, in: MWP 2017 - 2017 Int. Top. Meet. Microw. Photonics, Dec. 2017, pp. 1–4.

[17] S. Song, S.X. Chew, X. Yi, L. Nguyen, R.A. Minasian, Tunable single-passband microwave photonic filter based on integrated optical double notch filter, J. Lightwave Technol. 36 (19) (2018) 4557–4564.

[18] S. Sharma, S. Roy, A survey on design and synthesis techniques for photonic integrated circuits, J. Supercomput. 77 (5) (2021) 4332–4374.

[19] K.A. Van Vey, Optical Microring Resonators: Theory, Techniques, and Applications, CRC Press, Taylor and Francis Group, Boca Raton, FL, 2018.

[20] N. Kohli, B.L. Sang, F. Nabki, M. Ménard, Tunable bandpass filter with serially coupled ring resonators assisted MZI, IEEE Photonics J. 13 (4) (2021) 1–8.

[21] I. Krasnokutska, J.-L.J. Tambasco, A. Peruzzo, Large free spectral range microring resonators in lithium niobate on insulator, 2018.

[22] S. Radosavljevic, N.T. Beneitez, A. Katumba, M. Muneeb, M. Vanslembrouck, B. Kuyken, G. Roelkens, Mid-infrared Vernier racetrack resonator tunable filter implemented on a germanium on SOI waveguide platform, Opt. Mater. Express 8 (4) (2018) 824–835.

[23] W. Xie, L. Chang, H. Shu, J.C. Norman, J.D. Peters, X. Wang, J.E. Bowers, Ultrahigh-Q AlGaAs-on-insulator microresonators for integrated nonlinear photonics, Opt. Express 28 (22) (2020) 32894–32906.

[24] R. Marchetti, V. Vitali, C. Lacava, I. Cristiani, G. Giuliani, V. Muffato, M. Fournier, S. Abrate, R. Gaudino, E. Temporiti, L. Carroll, P. Minzioni, Low-loss micro-resonator filters fabricated in silicon by CMOS-compatible lithographic techniques: design and characterization, Appl. Sci. 7 (2) (2017) 174, https://www.mdpi.com/2076-3417/7/2/174.

[25] T.Y.L. Ang, J.R. Ong, S.T. Lim, C.E. Png, X. Guo, H. Wang, Versatile Bezier bends for silicon photonics, in: 2017 Conference on Lasers and Electro-Optics Pacific Rim (CLEO-PR), 2017, pp. 1–2.

[26] G. Delphi, S. Olyaee, M. Seifouri, A. Bahabady, Design of low cross-talk and high-quality-factor 2-channel and 4-channel optical demultiplexers based on photonic crystal nano-ring resonator, Photonic Netw. Commun. 38 (2019) 250–257.

[27] J. Zhang, H. Liu, Y. Ding, Y. Wang, A novel photonic crystal ring resonator configuration for add/drop filtering, Photonics Nanostruct. Fundam. Appl. 30 (2018) 14–19.

[28] Y. Xie, Z. Geng, D. Kong, L. Zhuang, A.J. Lowery, Selectable-FSR 10-GHz granularity WDM superchannel filter in a reconfigurable photonic integrated circuit, J. Lightwave Technol. 36 (13) (2018) 2619–2626.

[29] M. Bahadoran, I. Sadegh Amiri, Double critical coupled ring resonator-based add–drop filters, J. Theor. Appl. Phys. 13 (2019) 213–220.

[30] H. Han, B. Xiang, Simulation and analysis of electro-optic tunable microring resonators in silicon thin film on lithium niobate, Sci. Rep. 9 (2019) 6302.

[31] M. Milanizadeh, M. Petrini, F. Morichetti, A. Melloni, Polarization-transparent FSR-free microring resonator filter with wide hitless tunability, in: Optical Fiber Communication Conference, Optical Society of America, 2021, Tu6A–4.

[32] F. Dell'Olio, D. Conteduca, G. Brunetti, M.N. Armenise, C. Ciminelli, Novel CMOS-compatible athermal and polarization-insensitive ring resonator as photonic notch filter, IEEE Photonics J. 10 (6) (2018) 1–11.

[33] C.-L. Wu, Y.-J. Hung, R. Fan, D.-H. Ou, J.-Y. Huang, T.-H. Yen, Y.-J. Chiu, M.-H. Shih, Y.-Y. Lin, A.-K. Chu, C.-K. Lee, Tantalum pentoxide (Ta2O5) based athermal micro-ring resonator, OSA Contin. 2 (2019) 1198.

[34] T. Hiraki, T. Aihara, H. Nishi, T. Tsuchizawa, Deuterated SiN/SiON waveguides on Si platform and their application to C-band WDM filters, IEEE Photonics J. 9 (5) (2017) 1–7.

[35] A. Bagheri, F. Nazari, M.K. Moravvej-Farshi, Tunable optical demultiplexer for dense wavelength division multiplexing systems using graphene–silicon microring resonators, J. Electron. Mater. 49 (12) (2020) 7410–7419.

[36] T.J. Zimmerling, Y. Ren, D. Perron, V. Van, Sixth-order 2D microring optical filter with sharp transmission zero, in: 2019 Conf. Lasers Electro-Optics Eur. Eur. Quantum Electron. Conf., CLEO/Europe-EQEC 2019 23 (15) (2019) 1.

[37] J. Giron-Sierra, Digital Signal Processing with Matlab Examples, vol. 1, Springer, 2017.

[38] F. Xia, M. Rooks, L. Sekaric, Y. Vlasov, Ultra-compact high order ring resonator filters using submicron silicon photonic wires for on-chip optical interconnects, Opt. Express 15 (2007) 11934–11941.

[39] R. Maram, S. Kaushal, J. Azaña, L. Chen, Recent trends and advances of silicon-based integrated microwave photonics, Photonics 6 (2019) 13.

[40] D. Bonneau, J.W. Silverstone, M.G. Thompson, Silicon Quantum Photonics III: Systems and Applications, Springer, Berlin, Heidelberg, 2016.

[41] S. Miller, Y.H. Daniel Lee, J. Cardenas, A.L. Gaeta, M. Lipson, Electro-optic effect in silicon nitride, in: Conference on Lasers and Electro-Optics Europe - Technical Digest 2015, Aug. 2015, pp. 3–4.

[42] A.N.R. Ahmed, S. Shi, M. Zablocki, P. Yao, D.W. Prather, Tunable hybrid silicon nitride and thin-film lithium niobate electro-optic microresonator, Opt. Lett. 44 (3) (2019) 618–621, http://opg.optica.org/ol/abstract.cfm?URI=ol-44-3-618.

[43] F. Qiu, A. Spring, S. Yokoyama, Athermal and high-Q hybrid TiO2–Si3N4 ring resonator via an etching-free fabrication technique, ACS Photonics 2 (2015) 405–409.

[44] M. Bahadori, M. Nikdast, S. Rumley, L.Y. Dai, N. Janosik, T. Van Vaerenbergh, A. Gazman, Q. Cheng, R. Polster, K. Bergman, Design space exploration of microring resonators in silicon photonic interconnects: impact of the ring curvature, J. Lightwave Technol. 36 (13) (2018) 2767–2782.

[45] M.A. Rahman, A. Agrawal, Finite Element Modeling Methods for Photonics, Artech House, 2013.

[46] N. Cheplagin, G. Zaretskaya, Dispersion properties of uniform trapezoidal optical waveguides, J. Phys. Conf. Ser. 1400 (2019) 066041.

[47] P.O. Weigel, F. Valdez, J. Zhao, H. Li, S. Mookherjea, Design of high-bandwidth, low-voltage and low-loss hybrid lithium niobate electro-optic modulators, J. Phys.: Photonics 3 (1) (2020) 012001.

[48] N. Ahmed, S. Nelan, S. Shi, P. Yao, A. Mercante, D. Prather, Sub-volt electro-optical modulator on thin-film lithium niobate and silicon nitride hybrid platform, Opt. Lett. 45 (5) (2020) 1112–1115.

[49] P. Zhang, H. Huang, Y. Jiang, X. Han, H. Xiao, A. Frigg, T.G. Nguyen, A. Boes, G. Ren, Y. Su, Y. Tian, A. Mitchell, High-speed electro-optic modulator based on silicon nitride loaded lithium niobate on an insulator platform, Opt. Lett. 46 (23) (2021) 5986–5989, http://opg.optica.org/ol/abstract.cfm?URI=ol-46-23-5986.

[50] Z. Chang, W. Jin, K.S. Chiang, Graphene electrodes for lithium-niobate electro-optic devices, Opt. Lett. 43 (8) (2018) 1718–1721, http://opg.optica.org/ol/abstract.cfm?URI=ol-43-8-1718.